JGR Oceans

RESEARCH ARTICLE
10.1029/2020JC016096

Special Section:
Contributions from the Physics of Estuaries and Coastal Seas meeting, 2018

Using Tracer Variance Decay to Quantify Variability of Salinity Mixing in the Hudson River Estuary

John C. Warner[1], W. Rockwell Geyer[2], David K. Ralston[2], and Tarandeep Kalra[3]

[1]Woods Hole Coastal and Marine Science Center, U.S. Geological Survey, Woods Hole, MA, USA, [2]Applied Ocean Physics and Engineering Department, Woods Hole Oceanographic Institution, Woods Hole, MA, USA, [3]Integrated Statistics, Contracted to the U.S Geological Survey, Woods Hole, MA, USA

Abstract The salinity structure in an estuary is controlled by time-dependent mixing processes. However, the locations and temporal variability of where significant mixing occurs is not well-understood. Here we utilize a tracer variance approach to demonstrate the spatial and temporal structure of salinity mixing in the Hudson River Estuary. We run a 4-month hydrodynamic simulation of the tides, currents, and salinity that captures the spring-neap tidal variability as well as wind-driven and freshwater flow events. On a spring-neap time scale, salinity variance dissipation (mixing) occurs predominantly during the transition from neap to spring tides. On a tidal time scale, 60% of the salinity variance dissipation occurs during ebb tides and 40% during flood tides. Spatially, mixing during ebbs occurs primarily where lateral bottom salinity fronts intersect the bed at the transition from the main channel to adjacent shoals. During ebbs, these lateral fronts form seaward of constrictions located at multiple locations along the estuary. During floods, mixing is generated by a shear layer elevated in the water column at the top of the mixed bottom boundary layer, where variations in the along channel density gradients locally enhance the baroclinic pressure gradient leading to stronger vertical shear and more mixing. For both ebb and flood, the mixing occurs at the location of overlap of strong vertical stratification and eddy diffusivity, not at the maximum of either of those quantities. This understanding lends a new insight to the spatial and time dependence of the estuarine salinity structure.

Plain Language Summary The Hudson River Estuary is a location where salty ocean water mixes with fresh river water. The mixing of these different water sources occurs along the entire length of the estuary, with more mixing at certain locations at different times. In this study we study where and when the mixing occurs. It was found that there are certain locations that create more mixing due to changes in the channel width and the shape of the channel cross-section. More mixing occurred on the ebb tides than on the flood. This is important to understand how salt is mixed out of the estuary because these processes also control transport of other tracers in the estuary, as well as help us understand how changes to the estuary (like channel dredging or sea level rise) will affect salt intrusion.

Key Points:

- Greater mixing during ebb (average 60% of total) than flood (40% of total)
- Mixing occurs at fronts where strong stratification and active turbulence overlap
- Tracer variance approach directly quantifies spatial and temporal distribution of mixing

Correspondence to:
J. C. Warner,
jcwarner@usgs.gov

Citation:
Warner, J. C., Geyer, W. R., Ralston, D. K., & Kalra, T. (2020). Using tracer variance decay to quantify variability of salinity mixing in the Hudson River Estuary. *Journal of Geophysical Research: Oceans*, *125*, e2020JC016096. https://doi.org/10.1029/2020JC016096

Received 1 MAR 2020
Accepted 6 NOV 2020

1. Introduction

The salinity distribution in estuaries is controlled by the mixing of salt and fresh water, which is driven by many factors including tidal amplitude, freshwater inflow, bathymetry, wind stress, and waves. The timing and location of the mixing are dependent on stratification and shear in the water column, which vary tidally (Simpson et al., 1990) and over the spring neap cycle (Bowen & Geyer, 2003). There have been many previous approaches to identify and quantify the mechanisms of estuarine mixing. Early studies focused on constant and parameterized values of eddy diffusivity (Hansen & Rattray, 1965; Lerczak et al. 2006). However, the eddy diffusivity is not in itself a measure of estuarine mixing but rather of the turbulence that would cause mixing in the presence of a vertical gradient. Several recent studies of estuarine mixing (Burchard & Rennau, 2008; MacCready et al., 2018; Wang & Geyer, 2018) have proposed that the destruction of salinity variance provides the appropriate measure of the mixing of salt in an estuary. This destruction of scalar variance has long been addressed in context with turbulent microstructure as the quantity χ_s (Nash & Moum, 2002). Not only does χ_s relate directly to the irreversible process that formally represents mixing (in context with the entropy of mixing, Gregg, 1984), but it also has particular significance in context with estuaries in that the strength of the exchange flow is directly proportional to the volume integral of χ_s (MacCready et al., 2018).

The application of scalar mixing to estuaries was also applied in context with quantifying numerical mixing by Burchard and Rennau (2008), who used the volume integral of χ_s as a measure of the physical mixing with application to the Baltic Sea. MacCready et al. (2018) linked the integrated mixing to the exchange flow, applying the venerable Knudsen relation (Knudsen, 1900) to the quantification of estuarine mixing. Wang and Geyer (2018) demonstrated that not only is salinity variance useful for quantifying average mixing rates, it is also useful for examining the spatial and temporal variability of mixing.

This study utilizes the tracer variance approach to quantify the spatial and temporal variability of salinity mixing in the Hudson River estuary. The processes that create the mixing are identified and described. This approach builds on the results of Wang and Geyer (2018), who also used variance conservation to address mixing in the Hudson estuary. They related salinity variance to exchange flow and described the broad scale evolution of the salinity variance over the spring neap cycle. This study advances those findings to provide a more detailed examination of the temporal variability of tidal and spring neap time scales as well as spatial variability of where the mixing occurs, and it examines the physical processes responsible for mixing. The study is outlined with Section 2 describing the methods, Section 3 results, and Section 4 summary and discussion.

2. Methods

2.1. Observations

The Hudson River Estuary is located on the east coast of the United States and extends northward from New York Harbor to the Federal Dam in Troy, NY (Figure 1). North of the dam the major sources of fresh water are from the Upper Hudson and Mohawk Rivers, and the Estuary also receives lateral inflows that can increase the flow up to 50% (Wall et al., 2008). The mean summer (low flow) conditions can approach 200 m^3s^{-1} and maximum peak seasonal releases can reach up to 2,000 m^3s^{-1}. Peak to trough tidal range is about 2 m during spring tides, and depth-mean tidal velocities reach 1 ms^{-1} during spring tides. The landward extent of salt can reach up to 140 km or as little as 30 km north of Battery depending on freshwater discharge (Abood, 1974; de Vries & Weiss, 2001; Wells & Young, 1992).

The estuary has been the location of numerous previous observational and numerical investigations. A previous data collection program (Lerczak et al., 2009; Ralston et al., 2008) explored the tidal and subtidal salinity structure of the estuary and provided a comprehensive collection of observations during the spring and summer of 2004 that is used for this investigation. Some of the data collected included salinity, currents, and water levels that were measured with acoustic Doppler current profilers mounted on bottom tripods, and conductivity-temperature sensors on bottom tripods and on near surface buoys. Equipment was deployed at multiple stations along the thalweg of Hudson River (Figure 1), starting from the Battery (river km 0) and with stations at Lincoln Harbor (river km 5), Spuyten Duyvil (river km 22), Hastings (river km 33), Tappan Zee (river km 45), Croton Point (river km 55), and Bear Mountain (river km 77). Additionally, water level data from the U.S. Geological Survey (USGS) station at Poughkeepsie (https://waterdata.usgs.gov/nwis/uv?site_no=01372043), and water level and salinity measurements from the USGS at West Point (https://waterdata.usgs.gov/ny/nwis/uv/?site_no=01374019), and NOAA tides at Battery (https://tidesandcurrents.noaa.gov/stationhome.html?id=8518750) are utilized in this study.

2.2. Numerical Modeling

We use the Regional Ocean Modeling System (ROMS) to simulate the tidal hydrodynamics and salt transport in the study region for the observational time period. ROMS (Haidvogel et al., 2008; Shchepetkin & McWilliams, 2005) is a free-surface, explicit time stepping, structured grid numerical ocean model. This application is built on previous Hudson modeling efforts (Chen et al., 2012; Ralston & Geyer, 2019; Ralston et al., 2012, 2013, 2017; Wang et al., 2017; Warner et al., 2005, 2010), with a domain extending north to the tidal limit at Troy and expanded seaward to include New York Harbor and the East River. The grid is 530 cells in the x-direction and 1,100 in the y-direction, providing resolution on the order of 50–100 m laterally and 200 m in the along channel direction. Bathymetry was compiled from a combination of several

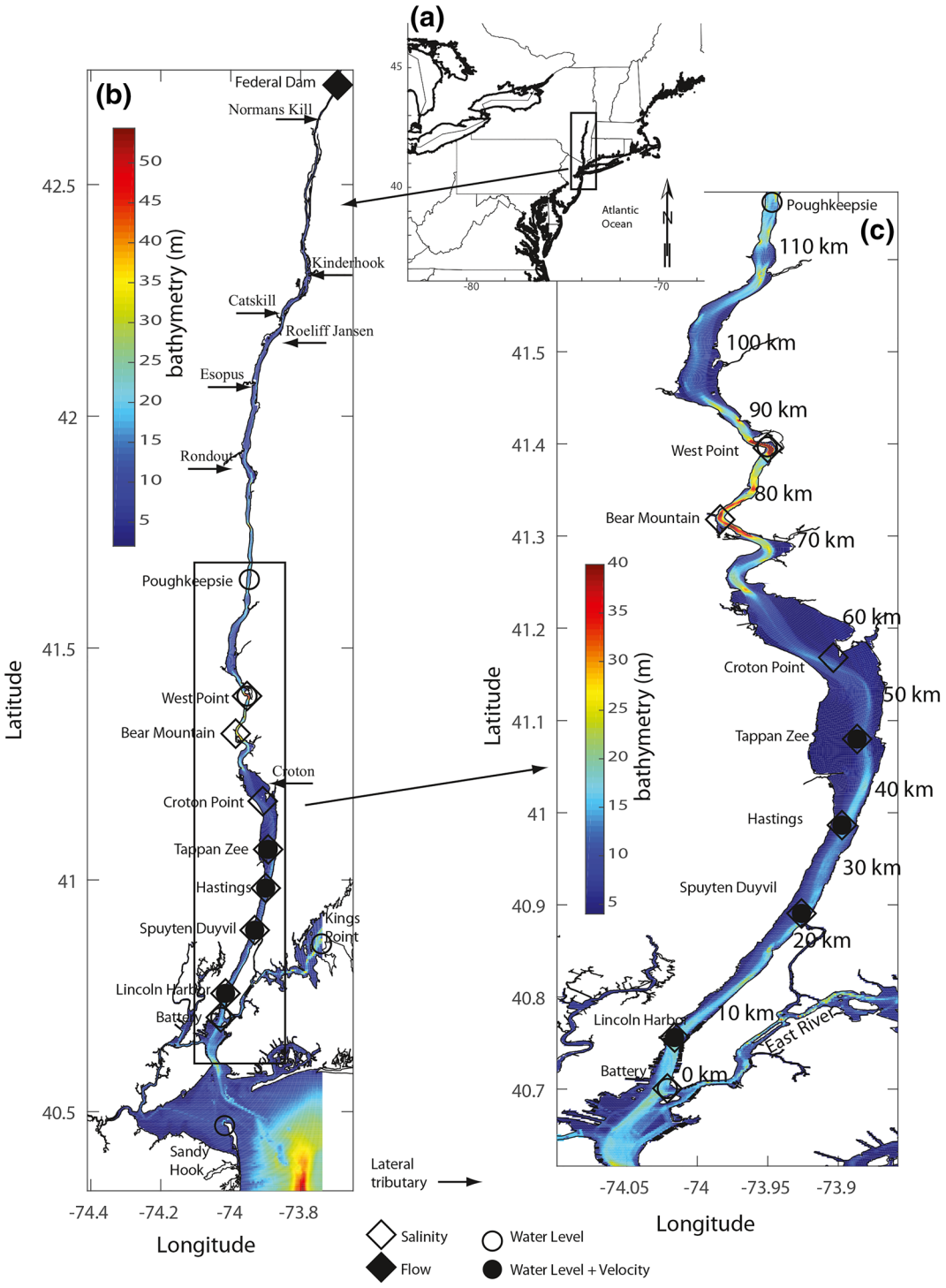

Figure 1. Hudson River numerical grid domain and bathymetry. (a) Location map for U.S. east coast. (b) Extent of full numerical grid using 532 cells in the x-direction and 1,135 cells in the y-direction. (c) Zoom in of lower estuary section, with grid cells sizes on the order of 50–100 m in the x-directions and 200 m in the y-directions.

sources including the Benthic Mapping Project by the New York State Department of Environmental Conservation (https://www.dec.ny.gov/imsmaps/benthic/webpages/index.html), digital elevation models from NOAA's National Center for Environmental Information (https://www.ngdc.noaa.gov/mgg/bathymetry/estuarine/), and the USGS Coastal National Elevation Database (https://www.usgs.gov/land-resources/eros/coned).

Boundary conditions at the northern end included freshwater input to the Hudson River as measured at the USGS stream gauge at Green Island, NY. Lateral tributaries along the tidal Hudson include flows from seven locations: Normans Kill, Kinderhook, Catskill, Roeliff Jansen, Esopus, Rondout, and Croton (Figure 1). These lateral flows contribute substantially to the total transport and have been shown to be essential for other tracers such as sediment (Ralston et al., 2012, 2013). For all inflows, the salinity was set to zero.

The eastern and southern boundaries were driven by a combination of tidal and subtidal water level variations. The tidal harmonics for these open boundaries were extracted from the ADCIRC tidal data base (Mukai et al., 2002) using nine harmonics (K1, O1, Q1, M2, S2, N2, K2, M4, and M6). In addition, subtidal water level variations were computed from observed time series of water level from NOAA tide gages at Kings Point, NY, and Sandy Hook, NJ (https://tidesandcurrents.noaa.gov/ports/stations 8516945 and 8531680). These water levels were low pass filtered to extract the low frequency storm component (periods > 30 h) and added along the open boundaries to account for offshore oceanic storm frequency band. Salinity along the open boundaries were imposed with constant values of 25 psu across the western end of Long Island Sound at Kings Points and a value of 30 psu along the open southern boundary to the Atlantic Ocean. A nudging time scale of 12 h was used with a radiation type boundary condition. This approach allowed the computed model salinity to radiate out of the domain during outflows and provided a smooth temporal transition for the salinity on inflow. The grid was extended into the Atlantic Ocean to provide a boundary location that was both distant (several tidal excursions) away from the study area and to a location of minimal salinity gradients. Variations to the nudging time scale on the order of hours did not modify the results. Wind speed and direction data from Newark Airport, Newark NJ (approx. 8 km from New York Harbor; https://www.ncdc.noaa.gov station GHCND:USW00014734) were used to compute a time-varying but spatially uniform surface momentum flux across the grid.

Initial conditions were zero velocity and water level. An initial salinity distribution was imposed based on previous simulations of the domain (Warner et al., 2010) by selecting a time period of similar river discharge and tidal amplitude. From this state, the model was simulated for an initial 21 days with river, tidal, and wind forcing to allow adjustments of the system to reach dynamic consistency. After that time, the model was simulated for another 115 days (136 days total). Only the last 115 days will be used for comparison and analysis in this study. The model was simulated with a time step of 5 s, using 16 uniformly spaced vertical levels, with a bottom roughness of $Z_0 = 0.002$ m, using the generic length scale (GLS) turbulence closure scheme and the Kantha-Clayson quasiequilibrium stability functions. A small horizontal viscosity (for momentum) was added of 0.25 m^2s^{-1} for numerical stability (mostly required in the not-well resolved regions of the East River with extremely high velocities). No interior tracer mixing or nudging was applied. Results were saved every hour for analysis (Warner & Kalra, 2019).

2.3. Model Skill

Predictive skill is based on quantitative agreement between model and observations. Using a method presented by Wilmott (1981) we define

$$\text{Skill} = 1 - \frac{\sum \left| X_{\text{model}} - X_{\text{obs}} \right|^2}{\sum \left(\left| X_{\text{model}} - \overline{X_{\text{obs}}} \right| + \left| X_{\text{obs}} - \overline{X_{\text{obs}}} \right| \right)^2} \quad (1)$$

where X is the variable being compared (either from the model or observation) and with the overbar evaluated as the time mean. Perfect agreement between model results and observations will yield a skill of 1.0 and complete disagreement yields a skill of 0. Model skill is evaluated for water levels and salinity.

2.4. Salinity Variance

To determine where and when salt mixes in an estuary, we will use an equation that describes the evolution of the salinity variance in the system. The equation describes how the variance evolves in space and time, and how the variance is being destroyed by mixing. The evolution of tracer variance can be shown as (Burchard & Rennau, 2008):

$$\partial_t\left(s'\right)^2 + v_j\partial_j\left(s'\right)^2 - \partial_x\left(K_h\partial_x\left(s'\right)^2\right) - \partial_y\left(K_h\partial_y\left(s'\right)^2\right) - \partial_z\left(K_v\partial_z\left(s'\right)^2\right) = -2K_h\left(\partial_x\left(s'\right)^2\right)^2 - 2K_h\left(\partial_y\left(s'\right)^2\right)^2 - 2K_v\left(\partial_z\left(s'\right)^2\right)^2 \quad (2)$$

where $\left(s'\right)^2$ is the square of the salinity variance, $\left(s'\right)^2 = \left(s - \overline{s}\right)^2$, s *(x,y,z,t)* is any conservative tracer and here we focus on s = salinity, $\overline{s}$ is the mean salinity over the spatial domain at an instance in time, v is velocity vector, K_h is the horizontal diffusivity, K_v the vertical diffusivity for salinity mixing, j are the spatial directions (x-, y-, and z-), x and y are horizontal directions, z is the vertical direction. The square of the total salinity variance was computed as $\left(s'\right)^2 = \left(s - \overline{s}\right)^2$ and the mean salinity $\overline{s} = \int sdV \Big/ \int dV$.

On the left side of the equation, the first term is the tendency for the salinity variance, along with the advection of variance (second term) and the diffusion of salinity variance (third, fourth, and fifth terms). The right side has two horizontal dissipation terms and the vertical variance dissipation term. In this equation the horizontal terms are negligible for this application as no additional horizontal mixing of salinity (K_h) was added. Additionally, the left-hand side vertical diffusion term is usually small. The main balance of the tendency is with advection (acts to redistribute variance) and the vertical variance dissipation (acts as a dominant sink term; Burchard & Rennau, 2008; MacCready et al., 2018). The application of this equation entails taking the integral of the relation over the estuarine volume with open boundaries at the upstream riverine and downstream ocean ends. The resulting fundamental variance budget (MacCready et al., 2018) is then:

$$\frac{d}{dt}\int s'^2\, dV = -\int u_n s'^2\, dA_{\text{bndry}} - 2\int K_v\left(\partial_z s'\right)^2 dV \quad (3)$$

where u_n is the outward-normal velocity at the open boundaries (varying across each cross-section) over the open areas (A_{bndry}). In this simpler, integral form of the balance, the time evolution of the salinity variance is dominantly controlled by the advective inputs at the open boundaries and the resolved loss of vertical variance due to turbulent mixing. This last term is the salinity variance dissipation (decay) caused by mixing and is the main focus of the analysis. This approach allows computation of the mixing to be resolved spatially within the control volume rather than as a bulk total of the estuary.

3. Results

3.1. Water Levels

Water surface elevation time series (Figure 2) vary with semi-diurnal, spring/neap, and lower frequency oscillations due to open-ocean storm induced fluctuations. The spring tide range varies from about 2 m near Battery and to 1.5 m farther up the estuary. The model captures the amplitude and phase variability of the free surface dynamics in the domain. The model skill for the water levels are 0.92, 0.93, 0.94, and 0.89 for the Battery, Spuyten Duyvil, Tappan Zee, and Poughkeepsie. The lower score further up the domain is most likely due to reduced resolution and unresolved channel roughness.

3.2. Salinity

Salinity time series (Figure 3) demonstrate strong variability through the system both spatially and temporally due to tidal and riverine effects. Large freshwater inflows occurred near days 93, 103, and 142 with

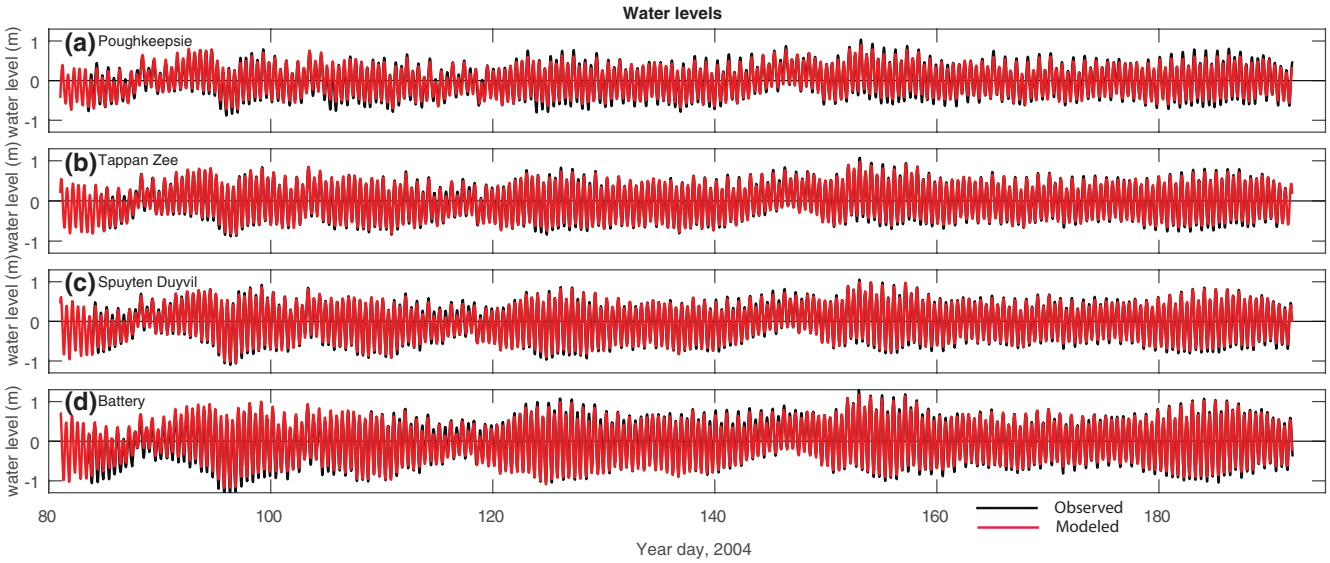

Figure 2. Time series of observed (black line) and modeled (red line) water levels at (a) Poughkeepsie; (b) Tappan Zee; (c) Spuyten Duyvil; (d) Battery.

flows approaching the typical peak discharge of 2,000 m^3s^{-1}, and in between events discharge was on the order of 500 m^3s^{-1}. Discharge decreased to about 250 m^3s^{-1} by the end of the study period.

At the Battery, near-bottom salinity varies from approximately 20–30 psu whereas surface salinity exhibits a greater range from near 5–20 psu. On a tidal time scale these near-surface salinity variations are on the order of 5 psu. At the spring-neap time scale, stratification ranges from less than 5 psu to over 20 psu. Further landward into the estuary, the effects of the spring/neap cycle become apparent in the salinity variability. The tidal energy is represented with the filtered value of the root-mean-square tidal amplitude (U_T, normalized to just show tidal energy). Neap tides (*N*) have lower tidal energy than spring tides (*S*). The first neap tide centered near day 90 was a period with extremely weak tides, reducing the amount of tidal mixing, and allowing landward salt intrusion beyond Bear Mountain (river km 77; Ralston et al., 2008). This reduced mixing allowed stratification of over 10 psu to develop through the majority of the estuary. Other neap tides centered on days 103, 118, 132, 145, 162, and 176 show similar response of increased stratification along the channel length, with reductions in stratification during spring tides. The variations are captured well by the model, with the exception of the first neap tide at the landward-most station of Bear Mountain. The model skill scores for the lower and upper sensors are 0.91 at the Battery, 0.86 and 0.93 at Lincoln Harbor, 0.89 and 0.95 at Spuyten Duyvil, 0.96 and 0.95 at Hastings, 0.96 and 0.95 at Tappan Zee, 0.92 and 0.95 at Croton Point, and 0.71 and 0.86 at Bear Mountain. As shown below, the majority of the salinity variance decay (mixing) occurs seaward of Tappan Zee. In this region the model has high skill even at Croton Point. Further landward the skill decreases most likely due to grid resolution and channel narrowing.

3.3. Salinity Variance

The salinity variance is computed for a control volume that extended from river kms 0 to 100. This contained the estuary region from the Battery to a location that was always landward of the farthest extent of salt intrusion. To compute the variance, first the mean salinity within this region is computed at each instant in time (Figure 4a). The mean salinity varies from a minimum value of around 3 psu during high discharge, to a maximum of near 10 psu. These instances of decreased mean occurred during spring tides and also during high discharge conditions. During neap tides and lower river discharge, especially near the end of the simulation period, the mean salinity increases because the volume of salt increases as the salinity intrusion moves landward.

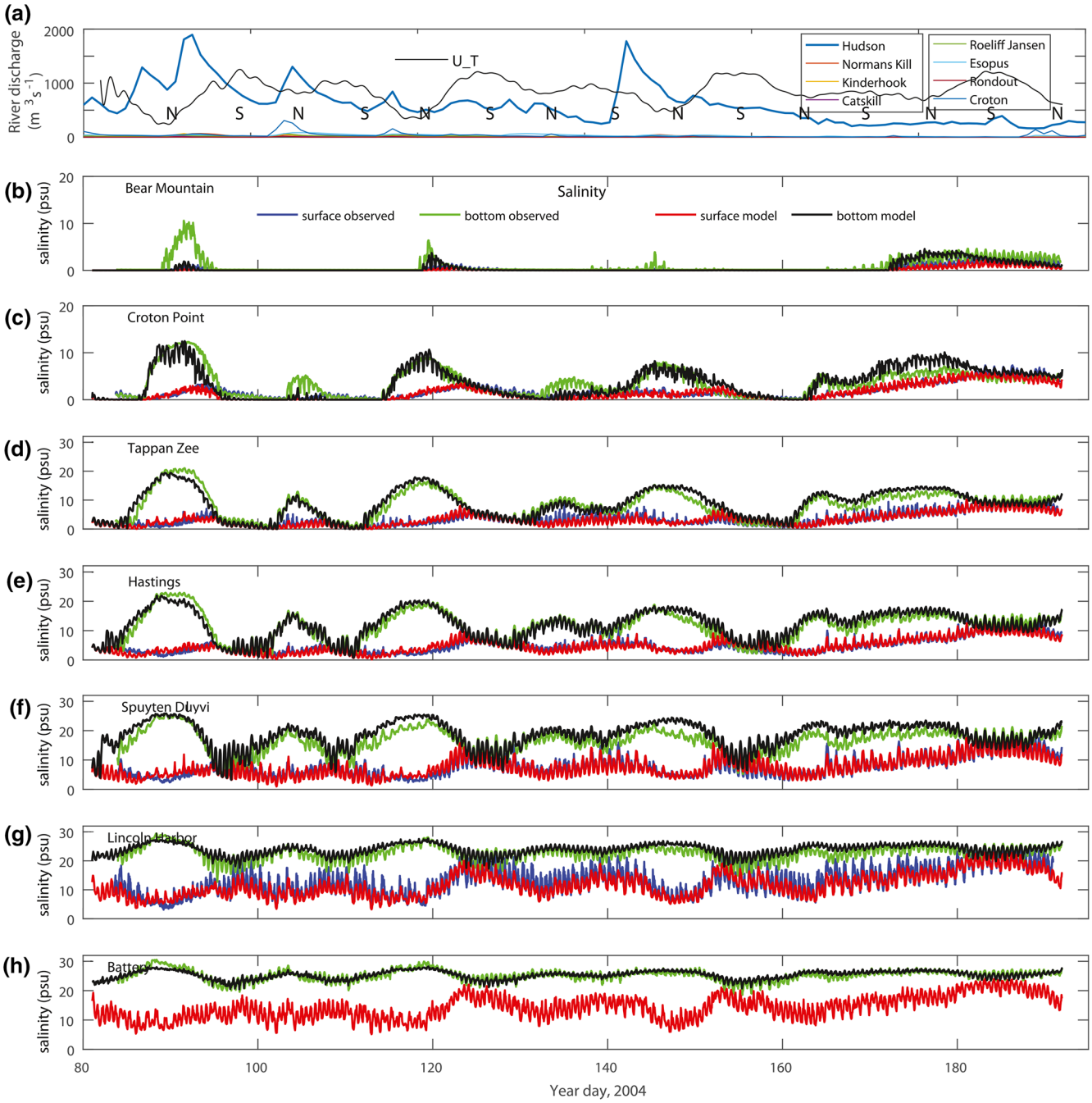

Figure 3. a) Time series of river flows and tidal amplitude (U_T) identifying spring (S) and neap (N) tides. Time series of near-bottom and surface salinity from the model and observed at locations along the estuary of (b) Bear Mountain, (c) Croton Point, (d) Tappan Zee, (e) Hastings, (f) Spuyten Duyvil, (g) Lincoln Harbor, and (h) Battery.

The salinity variance (Figure 4b, blue line) is computed at each time step by subtracting the mean salinity in the control volume from the salinity at each grid cell, squaring those residuals, and then taking the vertical and spatial mean. The total variance shows variations on both the tidal and spring/neap time scales. Tidally, the total variance changes on the order of 15 psu^2, which is approximately 25% of the mean total variance. This is due to the tidal advective term being a dominant factor in the variance balance (Figure 4c). At the spring-neap time scale, the total salinity variance is greater during neap tides than spring tides because of increased exchange flow at the open boundary that brings salinity variance into the estuary. The vertical

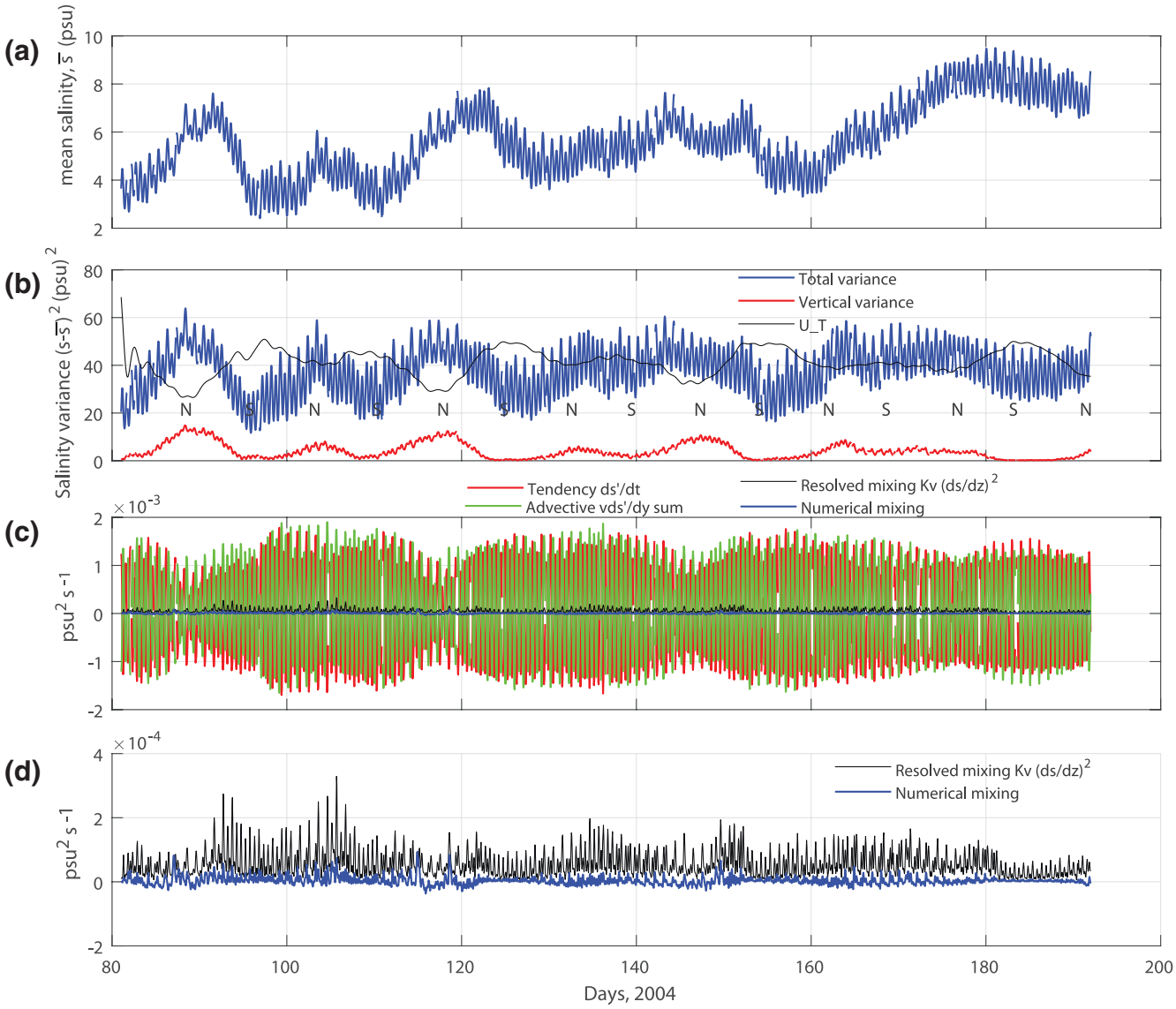

Figure 4. Time series of (a) mean salinity; (b) total and depth-averaged salinity variance; (c) terms of the salinity variance decay equation (tendency, advective, resolved mixing, and numerical mixing); and (d) zoom for the resolved mixing and numerical mixing.

variance is calculated in a similar manner to the total variance, except that the reference salinity is the local depth-mean rather than the mean salinity in the control volume. The vertical salinity variance reflects change in stratification, which increases during neap tides. Stratification is reduced during spring tides, and this decrease in both vertical and total variance is due to mixing.

Of the three main salinity variance terms of Equation 3, the tendency and the advective terms are dominant (Figure 4c). The advective term has a greater magnitude during spring tides due to transport of variance into and out of the domain at the seaward boundary, leading to large tidal variations in the tendency term. The flow that crosses the seaward boundary has vertical variations (and therefore variance), thus this transport is adding and removing variance on the tidal time scale. The resolved mixing (last term of Equation 3; Figure 4d) can reach up to 20% of the advective transport, but is more typically 10%–15%, and is largest during the transition from neap to spring tides. In addition, a measure of the numerical mixing was determined from the approach of Burchard and Rennau (2008). A further analysis on the numerical aspects of this approach is shown in Kalra et al. (2019). For this application to the Hudson River Estuary, the numerical

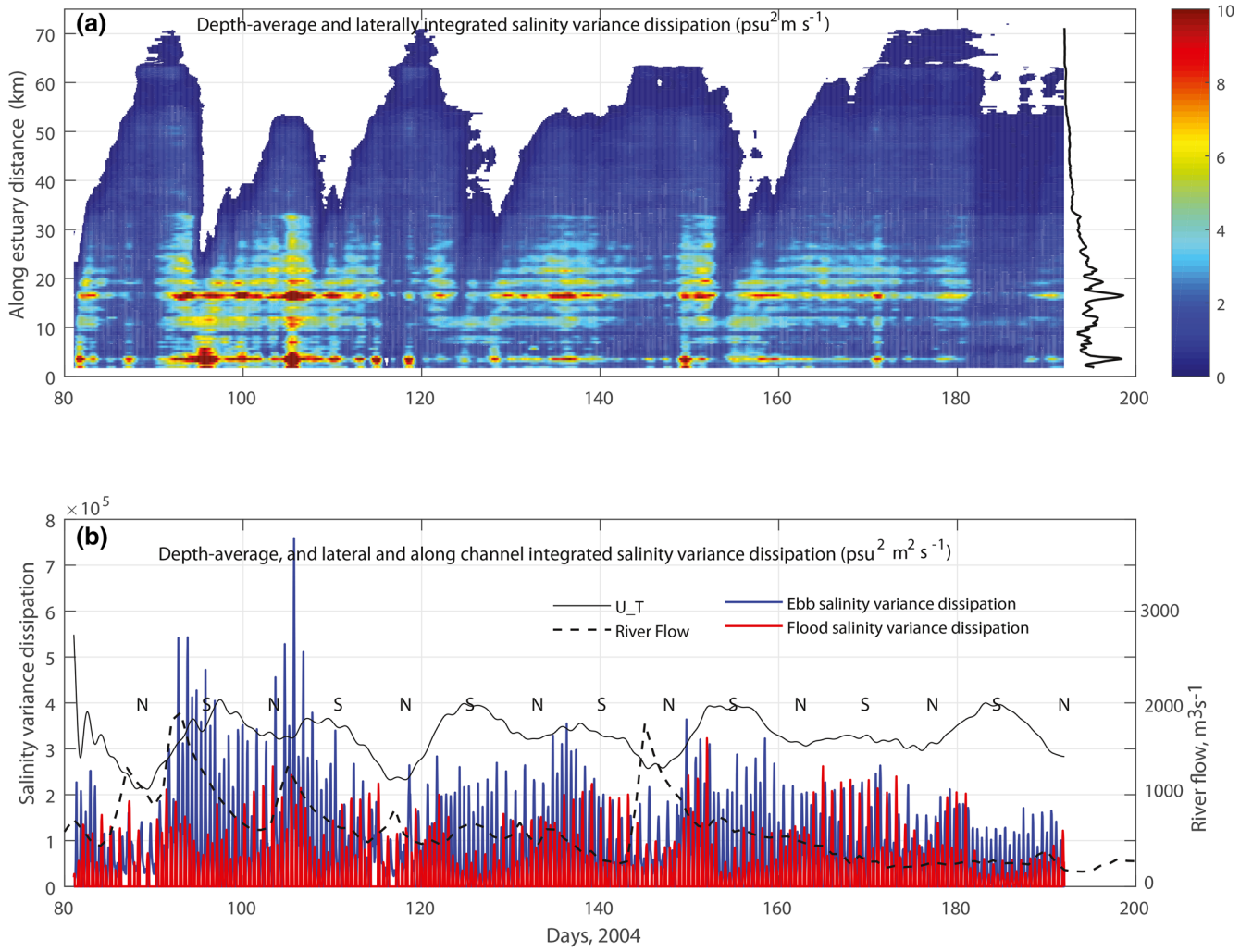

Figure 5. Time series of salinity dissipation for (a) depth-averaged and laterally integrated along-channel variation; and (b) ebb and flood total salinity variance dissipation (depth-averaged and lateral and along channel integrated), U_T measure for spring-neap cycle, and River flow.

mixing is calculated directly and found to be small. The numerical mixing is typically around 5% of the combined resolved plus numerical mixing, but can reach up to 15% of the total mixing (Figure 4d).

3.4. Salinity Variance Dissipation

The turbulent mixing is computed by the salinity variance dissipation term $-2K_v\left(\partial_z\left(s'\right)\right)^2$. Figure 5a shows the variations of this term, where, the salinity variance dissipation is depth averaged and laterally integrated and plotted along the length of the estuary. A 30-h temporal filter is applied to remove tidal variability and increase clarity. In the along estuary direction, the dissipation extends landward to the limit of salt intrusion, and beyond that there is no variance or dissipation of variance. This distance varies tidally but is predominately controlled by the spring-neap cycle and river discharge. The intrusion length is approximately in quadrature with the spring-neap cycle, with maximum landward intrusion during the neap to spring transition. The salt intrusion extends to a distance ranging from river kms 50 to 70 during the neap tides, and as short as to river km 25 during spring tides and increased river discharge. The dissipation occurs predominately in the lower section of the estuary that is relatively straight and narrow, seaward of river km 42. There is a peak in salinity variance dissipation near river km 18 during most of the simulation, and the temporal average dissipation (black line on right side Figure 5a) reflects this peak, in addition to local maxima at several other locations along the estuary (discussed in more detail below).

Integrating along the length of the estuary highlights the temporal variations of the salinity variance dissipation for ebb and flood (Figure 5b) tides. The total variance dissipation ranges from 1 to 8 $\times 10^5$ psu^{2}m^{2}s^{-1}. The total dissipation was divided up into ebb and flood periods (described below), and shows more dissipation during the ebbs than the floods. Ebb tide salinity variance dissipation is greater early in the time record, when there are stronger freshwater discharges and greater variability in the spring-neap cycle. Periods of increased dissipation occur after increased freshwater inflow because of the increased stratification and the opportunity for mixing. Comparing the salinity variance dissipation to the spring-neap variability in tidal velocity (U_T) shows that the dissipation typically increases during the transition from neap to spring as the becomes less stratified, as also shown in Wang and Geyer (2018).

Looking more closely on a shorter time scale of the tracer dissipation (21 day period from day 126–147) identifies more details of its along-channel and tidal characteristics. Figure 6a is the same as Figure 5a, now without the tidal filter, and zoomed in to show the tidal cycle during a neap-spring period. The salinity variance dissipation initially occurs primarily seaward of river km 30, but then it migrates landward with the salt intrusion during the neap tide. The mixing is often maximal near river km 18, but there are other locations such as river kms 4, 11, and 23 that show increased salinity variance dissipation. The local maxima are not constant in time, as the intensity of mixing varies tidally and over the spring neap cycle.

The along channel integrated variance dissipation (Figure 6b) shows the temporal behavior during ebbs (blue and shaded) and flood (red). The time periods chosen to define the flood and ebb phases were based on the modeled time series of depth-averaged velocity near the middle of the domain. Subsequent results are not sensitive to the exact timing of chosen flood and ebb periods. The ebb tides typically have a higher maximum dissipation, and the integrated total mixing is greater during the ebb tides than during the flood tides. Maximum salinity variance dissipation occurs during the ebbs from days 135 to 137, during the transition from neap to spring. There are periods with greater mixing during the flood tides than ebbs, especially following the spring tide near days 141–143. The flood tides with increased mixing (Figure 6c) tend to occur during periods of strong tidal diurnal inequality, and in particular during flood tides after very weak ebbs.

Summing the salinity variance dissipation for the different tidal phases reveals the spatial structure of mixing in the lower estuary. The sum for all the ebb tides (Figure 7a) shows a maximum located near river km 18. This is immediately south of a channel constriction and is at the location of the George Washington Bridge. There are other locations of increased mixing, such as from river kms 10 to 16 and from river kms 22 to 25. For the flood tides (Figure 7b), the average salinity variance dissipation shows locations of enhanced mixing that are different from the ebb regions. Flood tide mixing has a maximum near river km 20, immediately landward of the constriction at the George Washington Bridge. There are also other locations including along the western side of the channel from river kms 10 to 18, and along the eastern side of the channel from river kms 22 to 30.

The total (ebb + flood; Figure 7c) highlights distinctive zones of mixing along the estuary and demonstrates that mixing is not spatially uniform. The depth-averaged and laterally integrated mixing for the flood and ebb are plotted along the length of the estuary (Figure 7d). The minimum mixing rates are similar along the estuary for flood and ebbs (blue and red lines) but the localized regions of increased mixing often do not coincide. Zones of intensified ebb mixing are almost always greater than zones of intensified flood mixing along the estuary length. The ebb comprises ~60% of the total mixing with ~40% occurring during the flood. The cumulative sum (ebb + flood; dashed line Figure 7d) along the estuary shows that over the simulation period about 50% of the mixing occurs between the Battery and river km 20, and approximately 95% of the total mixing occurs below river km 40. This lower estuary region represents slightly over half the length of the salt intrusion during low discharge periods and neap tides.

3.5. Analysis of Mixing During Ebb Tides

The processes that create enhanced localized mixing during ebbs are demonstrated with a representative example from day 92 (Figure 8). Starting at the beginning of ebb, the near-bottom salinity is relatively uniform in the along channel direction. The bathymetry has a deeper channel on the east side and a shoal on the west, so the bottom water is fresher on the western shoal and saltier in the thalweg. Little mixing occurs at the beginning of ebb, with just a few small zones of enhanced dissipation along the western edge of the

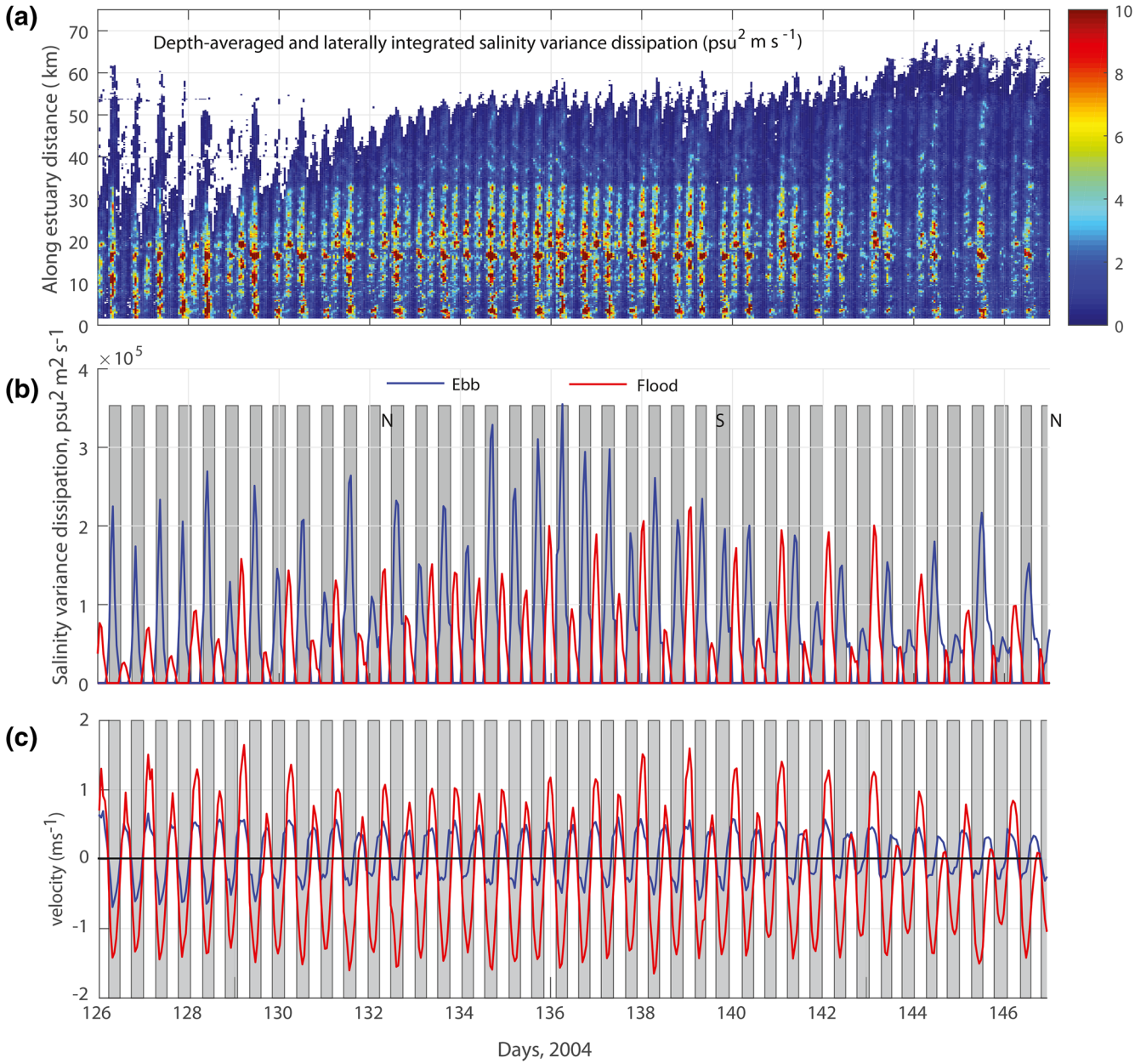

Figure 6. Tidal zoomed view. (a) Along channel variation of salinity variance dissipation during a Neap to Spring transition. (b) Along-channel integrated salinity variance dissipation showing tidal variations for ebb (blue) and flood (red) tidal periods; (c) tidal velocity showing surface (red) and bottom (blue) currents at a mid-estuary location.

channel (thick black outlined, Figure 8b). As the currents increase during ebb, differential advection between the lateral shoal and the slower moving water in the deeper part of the channel results in freshening of the bottom water to the west. Around max ebb (Figure 8, middle panels), localized lateral fronts begin to develop between the channel and shoal, and mixing increases along the western edge of the channel at the locations of the strong lateral gradients in salinity. During the late ebb (Figure 8, right panels), these lateral salinity gradients and regions of enhanced mixing persist. These locations of lateral fronts and mixing during this particular ebb coincide with the locations of enhanced mixing in the average over all ebbs (Figure 7a).

The link between the lateral fronts and enhanced mixing is through vertical variations of the pycnocline along the estuary. The isohaline structure can be seen in Figure 9 near maximum ebb (same time instance as

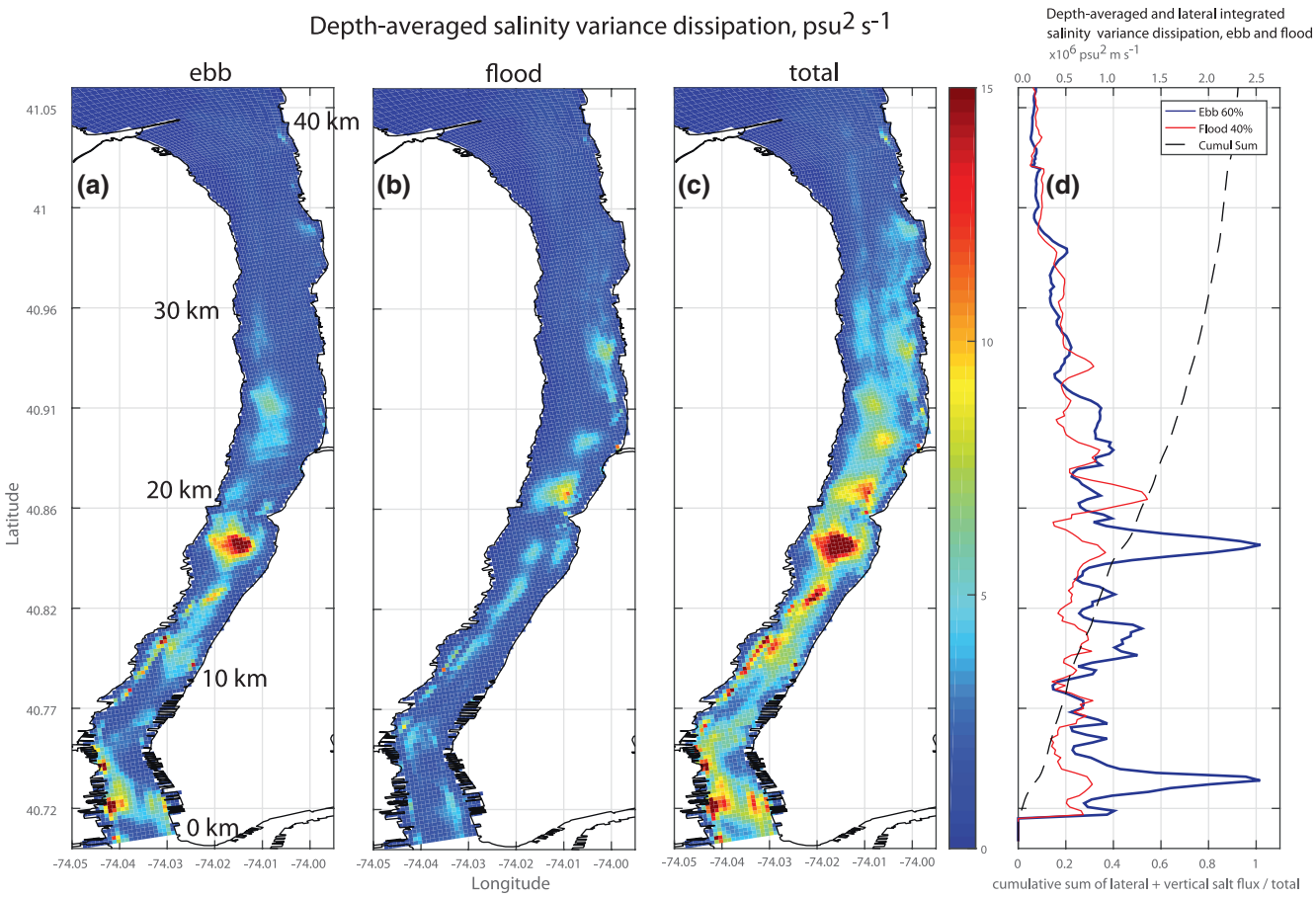

Figure 7. Depth-averaged salinity variance dissipation summed over 120 days during the (a) ebb tide; (b) flood tide; (c) total; (d) lateral sum for flood and ebb with percent total.

middle panels Figure 8). Here the depth of the 17 psu isohaline is used to represent the pycnocline, and the zones of enhanced mixing as shown in Figure 8 middle panels are also shown here in Figure 9 (outlined in black). The elevation of isohaline surface varies along the estuary, and the troughs and crests of the pycnocline are at an angle to main direction of flow. The isohaline intersects with the lateral shoal on the west side of the channel along an irregular path (dashed black line) due to variations of the height of the isohaline in response to lateral constrictions.

Two-layer hydraulic theory can be used to explain how along channel variations in geometry can modify the structure of stratified flows (Geyer & Ralston, 2011, 2015). During supercritical flow conditions (as is the case for most of the tidal cycle in the Hudson estuary, based on analysis by Geyer & Ralston 2015; Wang et al., 2017), at locations of lateral expansions the isohalines respond with an upward tilt (lifting in the downstream and ebb direction). Conversely, contractions cause downward tilt of the isohalines. The blue bands in Figure 9 correspond to depressions of the pycnocline that roughly correspond to changes in lateral width of the estuary (Geyer & Ralston, 2015). These depressions of the pycnocline intersect the shoal on the west side, resulting in oblique bottom fronts. These oblique bottom fronts coincide with the locations of increased mixing.

The location of maximum salinity variance dissipation is near river km 18. At this location, there is a bottom front that forms on the shoal during the mid-ebb. This can be seen in Figure 10 where we look at a section approximately normal to the front (location is shown in Figure 9). At the beginning of ebb, the isohalines (light gray contours) are almost level across this section (Figure 10, top panel). The stratification covers the majority of the water column extending from the free surface to nearly a depth of 10 m. The eddy diffusivity (black contours) is relatively low throughout the cross-section, with moderately greater values on the

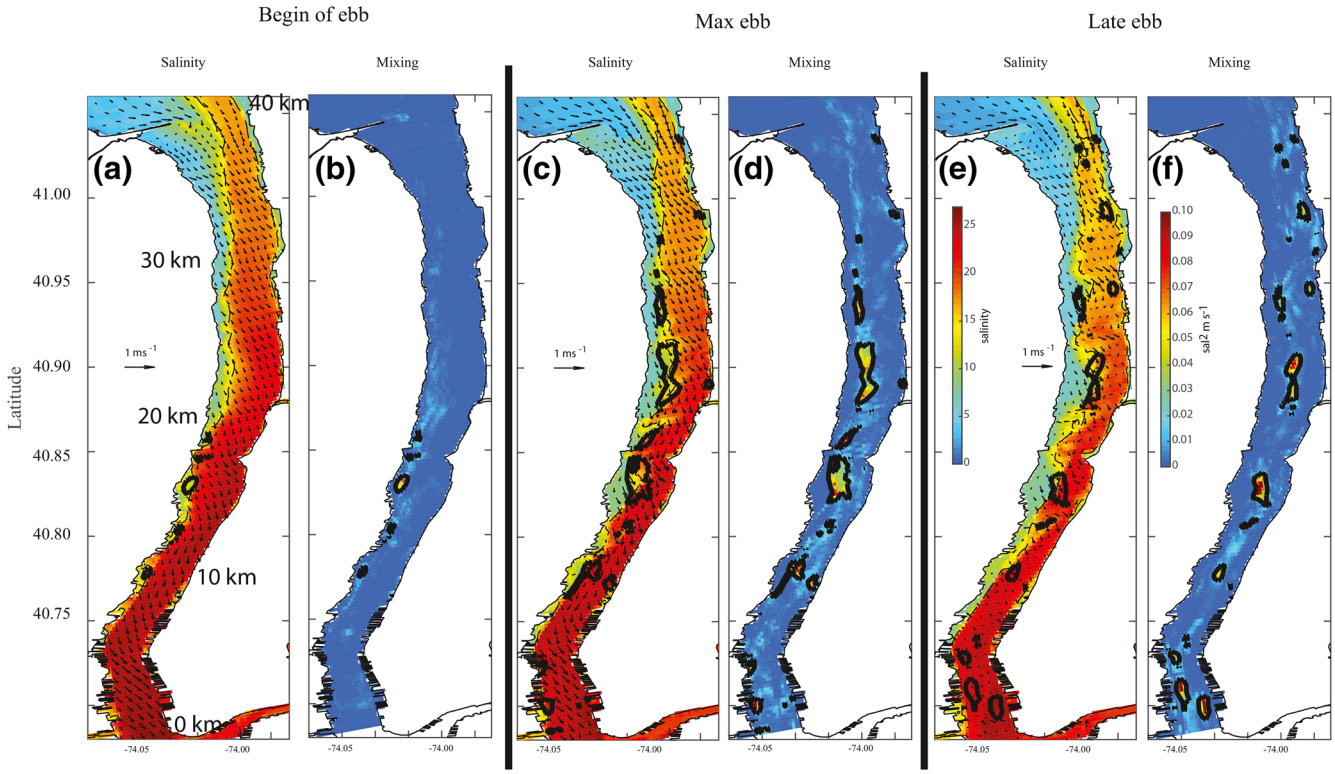

Figure 8. Three instances (beginning of ebb, max ebb, and late ebb) of salinity and salinity variance dissipation on day 92. Colors in left panels (a, c, e) are near-bottom salinity, and colors in right panels (b, d, f) are dissipation. Arrows are near-bottom velocity. Regions of maximum mixing are outlined in black on both panels.

western shoal. The salinity mixing (color shading) during the early ebb is small and confined to the shoal. By max ebb, mixing in the shallowest part of the shoal has destroyed the local stratification, and ebbing velocities have increased the eddy diffusivity (up to 0.03 m^2s^{-1}; Figure 10, middle panel). As described previously, tilting of the pycnocline causes the isohalines to intersect the bottom and create a lateral front. The stratification is now limited to the deeper part of the water column (right side of the figure). The mixing has a maximum value near the cross-front distance of 1,700 m. The location of maximum mixing occurs where the regions of high eddy diffusivity and stratification overlap, at the frontal location near the bed. At the end of ebb (Figure 10, bottom panel), the lateral front has moved deeper along the shoal. The location of maximum still occurs where the eddy diffusivity and stratification overlap, near the front where the isohalines bend downward toward the bed. There is no stratification on the lateral shoal (Figure 10, bottom panel), where the eddy diffusivity is greatest.

The cross-channel location of the lateral front is controlled by the mixing and lateral density gradient. As seen in Figure 10, bottom panel, the convergence of the isohalines near a cross-channel location at 2,000 m would drive a strong baroclinic pressure gradient toward the western shoal. However, on the shoal, it can be seen that the eddy diffusivity is large (0.03 m^2s^{-1}), and this mixing tends to erode the salt front, creating a balance on the shoal.

3.6. Analysis of Mixing During Flood Tides

The along channel variation of the salinity variance dissipation for the flood tides has a different structure than ebbs, as there are different dominant processes that control flood tide mixing. For the flood tides, the location of maximum dissipation occurs on the north side of the channel constriction near river km 20, near two other peaks at kms 18 and 22 (Figure 7). To examine the dominant mixing processes during flood tides, the along-estuary salinity structure is examined (Figure 11a) for a representative flood tide on day 103. Near

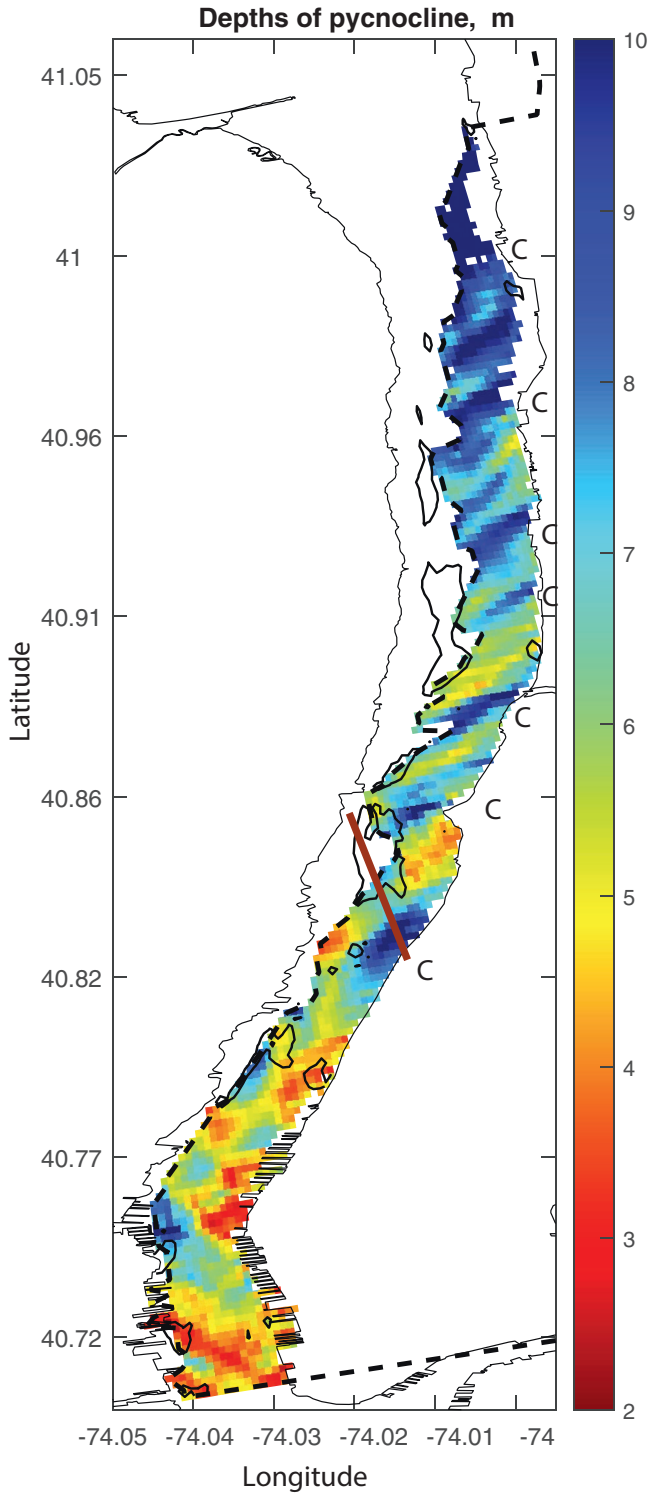

Figure 9. Depth of 17 psu salinity surface at max ebb (same time as Figure 8c). Dashed black lines shows intersection of isohaline and estuary bottom. Regions of maximum mixing (same as Figure 8d) are outlined in black. Channel constrictions labeled "C". Red line identifies cross-section location in Figure 10.

maximum flood, the salinity distribution shows a well-mixed bottom boundary layer (bbl) that extends vertically up to a depth of approximately −6 m along much of the lower estuary. The along-estuary variation in the elevation of the pycnocline, illustrated by select isohalines, reflects the influence of hydraulic response to the bathymetry. As shown in Geyer and Ralston (2015) and Geyer et al. (2017), when the composite Froude number (Froude number based on reduced gravity using density differences of the surface and bottom flow layers) is greater than 1, the vertical displacement of isohalines mirrors the bottom bathymetry contours. The influence of friction causes the isohaline response to the topography to be slightly out of phase and lagged seaward during flood tides. This topographically induced variation in the isohalines causes a change in sign of the baroclinic forcing between the upsloping and downsloping regions. In the downsloping zones, where the depth is increasing landwards, the baroclinic gradient has the same sense as the large-scale salinity gradient and acts to weakens the shear during the flood. However, in the upsloping zones, where the depth is decreasing landwards, the reversed baroclinic gradient (opposite baroclinic gradient than normally experienced in the estuary) enhances the flood-oriented shear. The flood shear is primarily driven by the bottom stress as the bottom boundary layer extends into the pycnocline, and this reversed baroclinic gradient is additive to that. This shear enhancement (Figure 11b) intensifies mixing by increasing turbulence production. Regions of enhanced mixing near river kms 18, 20, and 22 align with upsloping isohalines, with the maximum mixing localized near the top of the boundary layer. Similarly, the region of enhanced mixing at river kms 25–30 occurs near the top of the bottom boundary layer where the shear is favorable for enhanced turbulent kinetic energy production.

At times when the flood currents are weaker, the isohalines do not follow the bottom (not shown), including for example, during the weaker flood tides of the diurnal inequality (see Figure 6, days 140–146). During these weaker floods the upsloping pycnocline regions are not apparent and the shear and mixing near the top of the boundary layer is weak. The total salinity variance dissipation during these weaker floods is relatively limited.

The mixing processes for the flood tide are not isolated at a lateral front as during ebbs, but tend to extend across a significant fraction of the channel width (Figure 12). As with the ebb, the occurrence of strong mixing requires the combination of significant stratification and enhanced eddy diffusivity. At the beginning of the flood tide (Figure 12, top panel), in the cross-channel direction, the height of the bottom boundary layer is small and only covers the bottom few meters of the channel. The mixing is weak at this instance but it occurs at the top of the mixed layer. As the flood tide progresses the height of the bottom boundary layer increases with the 20 psu isohaline pushed up to being only 5 m below the surface and extending laterally across the entire section (Figure 12, middle panel). The maximum mixing is 0.025 $psu^2 s^{-1}$ (approximately the same magnitude as during the ebb). The stratification is larger and now is limited to the upper water column, where turbulence is too weak to contribute to significant mixing. The maximum eddy diffusivity is slightly less than near the beginning of the flood but covers a larger part of the cross-section because of the growth of the bottom boundary layer. The maximum mixing occurs in the region of overlap between stratification and eddy

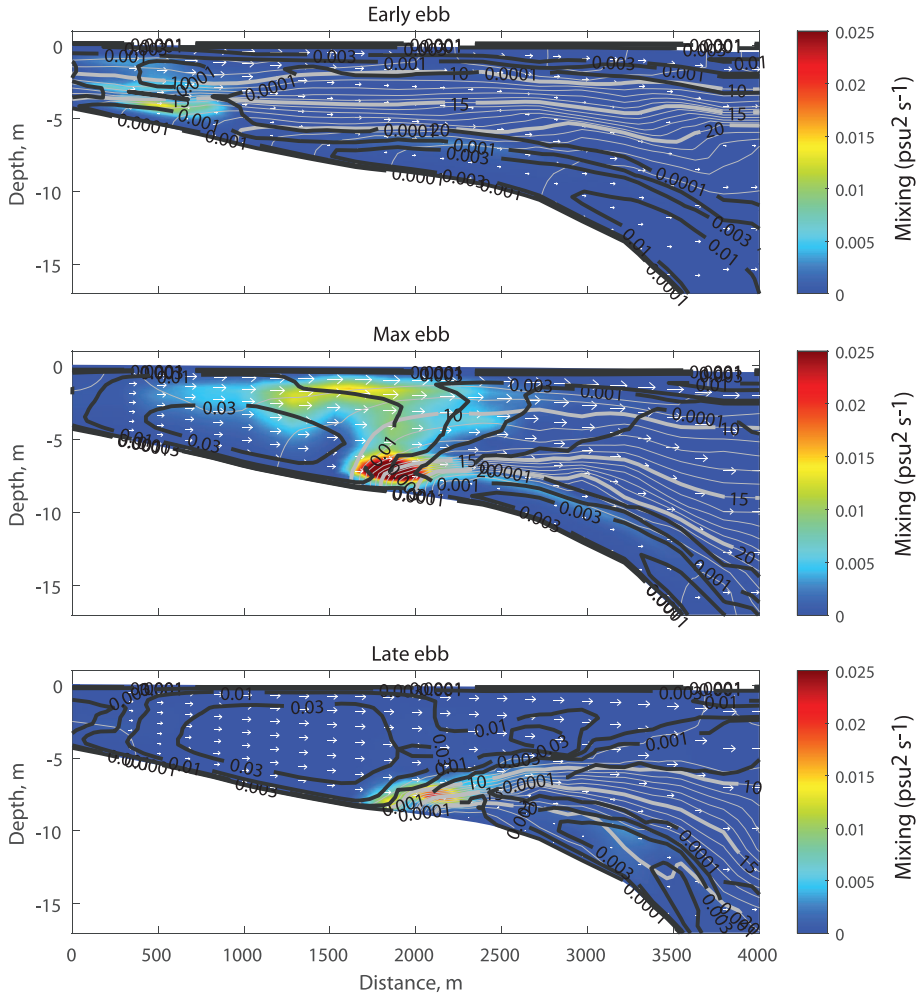

Figure 10. Cross sections of the salinity front at three time instances during ebb. Transect locations shown in Figure 9. Color shading is mixing (salinity variance dissipation), black contours are eddy diffusivity, and gray contours are isohalines.

diffusivity, not at the maximum of either of these two quantities. At the end of flood (Figure 12, bottom panel), dissipation at the top of the boundary layer has decreased in most of the cross-section, remaining greatest on the weakly stratified shoals.

4. Summary and Discussion

The tracer variance decay approach is a general method that can be used to identify locations in an estuary where mixing occurs. In this study, we used the dissipation of salinity variance to identify the temporal and spatial variability of mixing of salt, as salinity is the most important constituent in context with estuarine exchange flow (MacCready et al., 2018). In the Hudson River Estuary, it was found that mixing is intensified in locations with bathymetric variability along-estuary, with different primary mechanisms for ebb tides than for floods. During ebb, hydraulic response to lateral constrictions leads to bottom salinity fronts where the halocline impinges on the lateral shoal. The frontal regime provides a mechanism by which strong, boundary-generated turbulence impinges on the stratified waters near the frontal zone, resulting in efficient mixing. The combination of active turbulence and strong stratification within these frontal zones leads to the highest rates of mixing found in the estuary. The flood mixing is also spatially localized, but the mechanism is different from the ebb. The strongest mixing occurs where the baroclinic pressure gradient is reversed due to an upward-sloping halocline as a result of the hydraulic response to the along-estuary

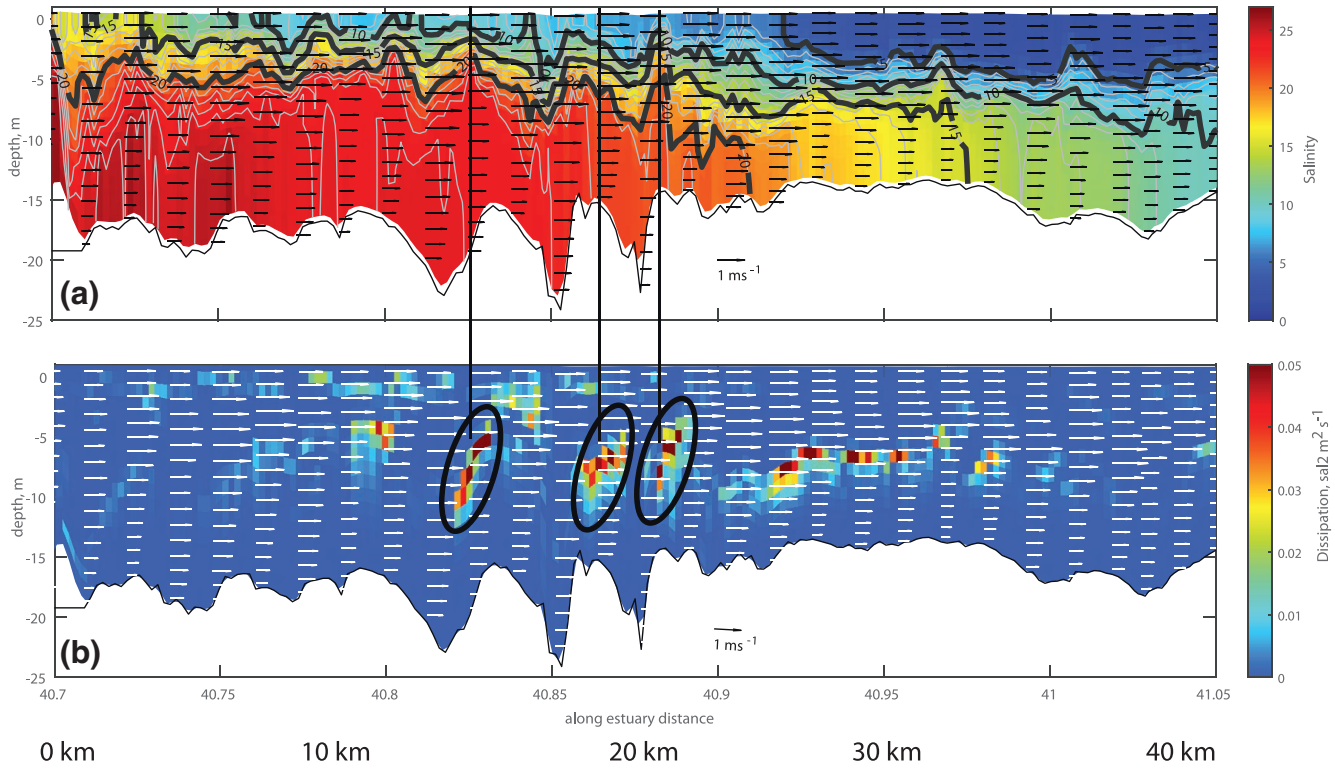

Figure 11. Maximum flood tide along-channel sections of (a) salinity and (b) salinity variance dissipation for instance of stronger flood current. Top panels show locations of steepened pycnocline correlate with zones of increased mixing.

bottom topography. This reversed baroclinicity enhances the shear in the upper part of the flood-directed boundary layer, causing enhanced turbulence production in the stratified, top portion of the boundary layer. Just as during the ebb, the coincidence of strong stratification and shear-generated turbulence are the critical ingredients for enhanced mixing.

The diurnal inequality of the tide in the Hudson creates asymmetry in the flood tide currents, and only the stronger flood tides initiated the mechanism for increased shear from adverse salinity gradient leading to more mixing. However, semi-diurnal variability in the mixing was less pronounced for the ebb currents, as the fronts can develop during most ebbs. For example, Figure 6b shows mixing during almost every ebb, but only has mixing for every other nonshaded flood tide. The integrated total mixing during the simulation period was greater during ebbs than floods, as was the maximum mixing intensity during most diurnal periods.

At the fortnightly time scale, the mixing was most significant during the neap to spring transition. This coincides with reduced stratification of the system and translation of the salt front seaward. The majority of the mixing occurred in the lower 30 km of the estuary, where strong stratification, significant tidal energy and topographic variability all contribute to localized hot-spots of mixing. Most estuaries have bathymetric variability at a range of spatial scales, and would also be expected to have similar temporal and spatial variability of mixing (Geyer & MacCready, 2014). The mixing processes occur at spatial scales corresponding with the local salinity gradients at fronts. These frontal scales are on the order of hundreds of meters, which is just being resolved by the current model grid configuration, but that suggests further investigations with increased resolution are merited to characterize the flow and bathymetric features that are producing the locally enhanced mixing.

Data Availability Statement

The model source code is available for download at https://code.usgs.gov/coawstmodel/COAWST and data sets discussed herein, and their associated metadata can be found in Warner and Kalra (2019).

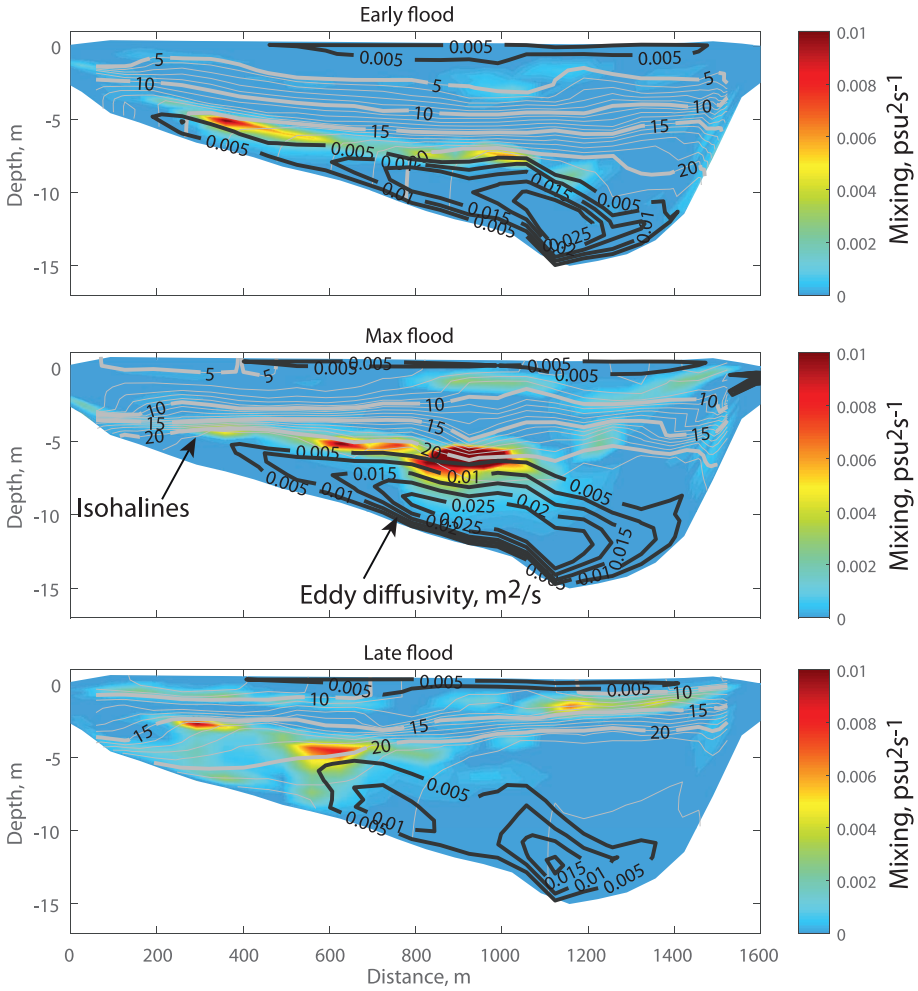

Figure 12. Cross-channel profiles for the development of flood tide mixing at river km 20. Color shading is mixing (salinity variance dissipation), black contours are eddy diffusivity, and gray contours are isohalines.

Acknowledgments
This study was funded through the Coastal Model Applications and Field Measurements Project and the Cross-shore and Inlets Project, US Geological Survey Coastal Marine Hazards and Resources Program. Any use of trade, firm, or product names is for descriptive purposes only and does not imply endorsement by the US Government.

References

Abood, K. A. (1974). Circulation in the Hudson estuary, *Annals of the New York Academy of Sciences*, *250*, 39–111.

Bowen, M. M., & Geyer, W. R. (2003). Salt transport and the time dependent salt balance of a partially stratified estuary. *Journal of Geophysical Research: Oceans*, *108*(C5), 3158. https://doi.org/10.1029/2001JC001231

Burchard, H., & Rennau, H. (2008). Comparative quantification of physically and numerically induced mixing in ocean models. *Ocean Modell*, *20*, 293–311. https://doi.org/10.1016/j.ocemod.2007.10.003

Chen, S., Geyer, W. R., Ralston, D. K., & Lerczak, J. A. (2012). Estuarine exchange flow quantified with isohaline coordinates: Contrasting long and short estuaries. *Journal of Physical Oceanography*, *42*, 748–763. https://doi.org/10.1175/JPO-D-11-086.1

de Vries, M. P., & Weiss, L. A. (2001). *Salt-front movement in the Hudson River estuary, New York—Simulations by one-dimensional flow and solute-transport models, U.S. Geological Survey*. (Water Resources Investigations Report 99–4024, p. 69). https://pubs.usgs.gov/wri/1999/4024/wri19994024.pdf

Geyer, W. R., & Ralston, D. K. (2011). The dynamics of strongly stratified estuaries, In Wolanski, E. & McLusky, D. S. (Eds.) Treatise on estuarine and coastal science (Vol. 2, pp. 37–51). Waltham, MA: Academic Press. https://doi.org/10.1016/B978-0-12-374711-2.00206-0

Geyer, W. R., & MacCready, P. (2014). The Estuarine Circulation. *Annual Review of Fluid Mechanics*, *46*, 175–197. https://doi.org/10.1146/annurev-fluid-010313-141302

Geyer, W. R., & Ralston, D. K. (2015). Estuarine frontogenesis, *Journal of Physical Oceanography*, *45*, 546–561. https://doi.org/10.1175/JPO-D-14-0082.1

Geyer, W. R., Ralston, D. K., & Holleman, R. C. (2017). Hydraulics and mixing in a laterally divergent channel of a highly stratified estuary. *Journal of Geophysical Research: Oceans*, *122*, 4743–4760. https://doi.org/10.1002/2016JC012455

Gregg, M. C. (1984). Entropy generation in the ocean by small-scale mixing. *Journal of Physical Oceanography*, *14*, 688–711.

Haidvogel, D. B., Arango, H., Budgell, W. P., Cornuelle, B. D., Curchitser, E., Di Lorenzo, E., et al. (2008), Ocean forecasting in terrain-following coordinates: Formulation and skill assessment of the Regional Ocean modeling system, *Journal of Computational Physics*, *227*(7), 3595–3624. https://doi.org/10.1016/j.jcp.2007.06.016

Hansen, D. V., & Rattray, M. (1965). Gravitational circulation in straits and estuaries. *Journal of Marine Research*, *23*, 104–122

Kalra, T. S., Li, X., Warner, J. C., Geyer, W. R., & Wu, H. (2019). Comparison of physical to numerical mixing with different tracer advection schemes in estuarine environments. *Journal of Marine Science and Engineering*, *7*, 338.

Knudsen, M. (1900). Ein hydrographischer Lehrsatz. *Annalen der Hydrographie und Maritimen Meteorologie*, *28*(7), 316–320 (in German)

Lerczak, J. A., Geyer, W. R., & Chant, R. J. (2006). Mechanisms driving the time-dependent salt flux in a partially stratified estuary. *Journal of Physical Oceanography*, *36*, 2296–2311. https://doi.org/10.1175/JPO2959.1

Lerczak, J. A., Geyer, W. R., & Ralston, D. K. (2009). The temporal response of the length of a partially stratified estuary to changes in river flow and tidal amplitude. *Journal of Physical Oceanography*, *39*, 915–933. https://doi.org/10.1175/2008JPO3933.1

MacCready, P., Geyer, W. R., & Burchard, H. (2018). Estuarine exchange flow is related to mixing through the salinity variance budget. *Journal of Physical Oceanography*, *48*, 1375–1384. https://doi.org/10.1175/JPO-D-17-0266.1

Mukai, A. Y., Westerink, J. J., Luettich, R. A., & Mark, D. J. (2002). *Eastcoast 2001, a tidal constituent database for the western North Atlantic, Gulf of Mexico and Caribbean Sea*. Vicksburg, MS: U.S. Army Engineer Research and Development Center. CIRP TR-02-24.

Nash, J., & Moum, J. (2002). Microstructure estimates of turbulent salinity flux and the dissipation spectrum of salinity. *Journal of Physical Oceanography*, *32*, 2312–2333. https://doi.org/10.1175/1520-0485(2002)032<2312:MEOTSF>2.0.CO;2

Ralston, D. K., Cowles, G. W., Geyer, W. R., & Holleman, R. C. (2017). Turbulent and numerical mixing in a salt wedge estuary: Dependence on grid resolution, bottom roughness, and turbulence closure. *Journal of Geophysical Research: Oceans*, *122*, 692–712. https://doi.org/10.1002/2016JC011738

Ralston, D. K., & Geyer, W. R. (2019). Response to channel deepening of the salinity intrusion, estuarine circulation, and stratification in an urbanized estuary. *Journal of Geophysical Research: Oceans*, *124*, 4784–4802. https://doi.org/10.1029/2019JC015006

Ralston, D. K., Geyer, W. R., & Lerczak, J. A. (2008). Subtidal salinity and velocity in the Hudson River estuary: Observations and modeling. *Journal of Physical Oceanography*, *38*, 753–770. https://doi.org/10.1175/2007JPO3808.1

Ralston, D. K., Geyer, W. R., & Warner, J. C. (2012). Bathymetric controls on sediment transport in the Hudson River estuary: Lateral asymmetry and frontal trapping, *Journal of Geophysical Research*, *117*, C10013. https://doi.org/10.1029/2012JC008124

Ralston, D. K., Warner, J. C., Geyer, W. R., & Wall, G. R. (2013). Sediment transport due to extreme events: The Hudson River estuary after tropical storms Irene and Lee. *Geophysical Research Letters*, *40*, 5451–5455. https://doi.org/10.1002/2013GL057906

Shchepetkin, A. F., & McWilliams, J. C. (2005). The regional oceanic modeling system (ROMS): A split-explicit, free-surface, topography-following-coordinate oceanic model, *Ocean Modelling*, *9*(4), 347–404. https://doi.org/10.1016/j.ocemod.2004.08.002

Simpson, J. H., Brown, J., Matthews, J., & Allen, G. (1990). Tidal straining, density currents, and stirring in the control of estuarine stratification. *Estuaries*, *13*, 125–132

Wall, G. R., Nystrom, E. A., & Litten, S. (2008). Suspended sediment transport in the freshwater reach of the Hudson River estuary in eastern New York. *Estuaries and Coasts*, *31*, 542. https://doi.org/10.1007/s12237-008-9050-y

Wang, T., & Geyer, W. R. (2018). The balance of salinity variance in a partially stratified estuary: Implications for exchange flow, mixing, and stratification. *Journal of Physical Oceanography*, *48*, 2887–2899. https://doi.org/10.1175/JPO-D-18-0032.1

Wang, T., Geyer, W. R., & MacCready, P. (2017). Total exchange flow, entrainment, and diffusive salt flux in estuaries. *Journal of Physical Oceanography*, *47*, 1205–1220. https://doi.org/10.1175/JPO-D-16-0258.1

Warner, J. C., Geyer, W. R., & Arango, H. G. (2010). Using a composite grid approach in a complex coastal domain to estimate estuarine residence time. *Computers and Geosciences*, *36*, 921–935.

Warner, J. C., Geyer, W. R., & Lerczak, J. A. (2005). Numerical modeling of an estuary: A comprehensive skill assessment, *Journal of Geophysical Research*, *110*, C05001. https://doi.org/10.1029/2004JC002691

Warner, J. C., & Kalra, T. S. (2019). *Numerical model of salinity transport and mixing in the Hudson River estuary*. Reston, VA: U.S. Geological Survey Data Release; USGS.

Wells, A. W., & Young, J. R. (1992). Long-term variability and predictability of Hudson River physical and chemical characteristics, In C. Lavett Smith (Ed.) *Estuarine research in the 1980s* (pp. 29–58). Albany, NY: State University of New York Press.

Wilmott, C. J. (1981). On the validation of models. *Physical Geography*, *2*, 184–194.